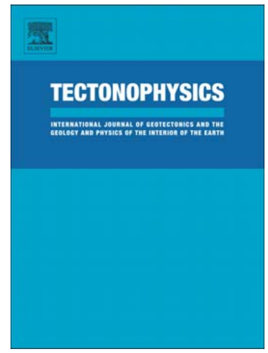

Accepted Manuscript

Plate boundary deformation in North Iceland during 1992-2009 revealed by InSAR time-series analysis and GPS

Sabrina Metzger, Sigurjón Jónsson

PII: S0040-1951(14)00407-7
DOI: doi: 10.1016/j.tecto.2014.07.027
Reference: TECTO 126402

To appear in: *Tectonophysics*

Received date: 23 January 2014
Revised date: 4 June 2014
Accepted date: 21 July 2014

Plate boundary deformation in North Iceland during 1992-2009 revealed by InSAR time-series analysis and GPS

Sabrina Metzger

Institute of Geophysics, ETH Zürich, Sonneggstrasse 5, 8092 Zürich, Switzerland,
Now at: German Research Centre for Geosciences, Telegraphenberg, 14473 Potsdam, Germany

Sigurjón Jónsson

King Abdullah University of Science and Technology, Thuwal, Saudi Arabia

Abstract

In North Iceland, extensional plate motion is accommodated by the Northern Volcanic Zone, a set of en-echelon volcanic systems, and the Tjörnes Fracture Zone, a transform offset in the mid-Atlantic Ridge consisting of two parallel transform lineaments. The southern lineament, the Húsavík-Flatey fault, is a 100 km-long right-lateral strike slip fault that has not ruptured for more than 140 years and poses a significant seismic hazard to Húsavík, a fishing town located by the fault, and to other coastal communities. We present results of InSAR time-series analysis data spanning almost two decades (1992 – 2009) that show extensional and interseismic deformation within the Northern Volcanic Zone and the on-shore part of the Tjörnes Fracture Zone. The results also exhibit transient inflation at Theistareykir volcano, deflation at Krafla central volcano and a broad uplift north of Krafla. The current plate extension is not uniform across the Northern Volcanic Zone, but concentrated at the western fissures of the Theistareykir volcanic system and the outermost fissures of the Krafla fissure swarm. We combine a back-slip plate boundary model with a set of point pressure sources representing volcanic changes to describe the current extensional plate boundary deformation and update the previous estimations of the locking depth and slip rate of the Húsavík-Flatey fault that were based on GPS data alone. Using different combinations of input data, we find that the Húsavík-Flatey fault has a locking depth of 6-10 km and, with a slip rate of 6-9 mm/yr, is accommodating about a third of the full transform motion. We furthermore show that while the InSAR data provide important constraints on the volcanic deformation within the NVZ, they do not significantly improve the model parameter estimation for the HFF, as the dense GPS network appears to better capture the defor-

Email address: metzger@gfz-potsdam.de (Sabrina Metzger)

mation across the fault.

Keywords: InSAR, time-series analysis, interseismic deformation, transform faults, kinematics of crustal and mantle deformation, Northern Volcanic Zone

1. Introduction

The Tjörnes Fracture Zone (TFZ) is a 120 km-offset in the mid-Atlantic Ridge that connects the onshore Northern Volcanic Zone (NVZ) to the offshore Kolbeinsey Ridge north of Iceland (Fig. 1). The transform motion of 18.4 $\pm$0.4 mm/yr (MORVEL, DeMets et al., 2010) is accommodated by two parallel lineaments, the Húsavík-Flatey fault (HFF) and the Grímsey Oblique Rift (GOR, Einarsson, 2008). The TFZ is mostly offshore, except for a small part of the HFF that cuts through the fishing town of Húsavík. No major earthquakes have occurred on the HFF since two magnitude 6.5 events struck the area in 1872 (Halldórsson, 2005). It is therefore of significant interest and importance to assess the slip rate and locking depth of the Húsavík-Flatey fault and thus the current interseismic strain accumulation rate. As the fault is linked to the active rifting segments in the NVZ, we also need to study the deformation within the NVZ to gain more insight into the rift-transform interaction and its influence on the fault loading.

In our previous work, we used Global Positioning System (GPS) time-series spanning thirteen years (1997-2010) to constrain parameters of a kinematic model of the plate boundary zone in North Iceland and estimate the seismic potential of the locked HFF to be equivalent to a M_w6.8$\pm$0.1 earthquake (Metzger et al., 2011, 2013). Our best-fit model slip rate for the HFF (6.8$\pm$0.3 mm/yr) indicated that only a third of the full transform motion is accommodated by the HFF, while the rest is focused on the GOR. We furthermore constrained the plate divergence rate at $20.3^{+0.4}_{-0.3}$ mm/yr, which is slightly higher than what is suggested by the MORVEL plate motion model. The higher rate was probably caused by unmodeled remains of the 1975-1984 Krafla rifting episode (de Zeeuw-van Dalfsen et al., 2004; Árnadóttir et al., 2009; Pedersen et al., 2009) that impacted the first part of the GPS time-series (Völksen, 2000; Jouanne et al., 2006). We estimated the locking depth of the HFF to be shallow, at $6.2^{+0.8}_{-0.7}$ km, which may be the result of the anomalous high temperature gradient in Iceland (Flóvenz and Sæmundsson, 1993). This determination of the fault slip rate and locking depth marked a significant improvement to previous fault-parameter estimates for the HFF (e.g. Jouanne et al., 2006; Árnadóttir et al., 2009) in terms of accuracy and amount of near-field input data. The interseismic model parameters compare well with the outcome of similar models of south Iceland (LaFemina et al., 2005; Árnadóttir et al., 2006; Geirsson et al., 2012). Furthermore, we showed that by adding the data from 44 campaign GPS sites to the initial data set from fifteen continuous GPS stations (Metzger et al., 2011), we reduce the statistical uncertainties of the estimated model parameters by at least 50 % (Metzger et al., 2013). The uncertainty ranges have become so small that the influence of the model choice outweighs the influence of the data uncertainties.

Interferometric synthetic aperture radar (InSAR) studies of North Iceland have focused mostly on local volcanic deformation such as the deformation after the Krafla rifting episode that ended in 1984 (Sigmundsson et al., 1997), the detection of a broad uplift north of Krafla between 1993 and 1999 (de Zeeuw-van Dalfsen et al., 2004) and the recent inflation of Theistareykir in 2007-2009 (Metzger et al., 2011, 2013; Spaans et al., 2012). Pedersen et al. (2009) described the inter-rifting deformation taking place in the NVZ by using 2D and 3D finite element models. They used a set of interferograms covering the Askja and Krafla volcanic systems and found that the vertical deformation seems to be confined within the recently active fissure swarms, whereas horizontal deformation is distributed over a broader zone.

In this paper, we present the first InSAR time-series analysis of the region that links the NVZ and the Tjörnes Fracture Zone in order to assess the plate-boundary deformation on a larger scale and to constrain better the shear deformation across the locked HFF. Our InSAR time-series data span nearly two decades (1992 – 2009) and cover the onshore part of the Tjörnes Fracture Zone and the northern part of the NVZ, including the Theistareykir and Krafla central volcanoes. We use 92 European Remote Sensing (ERS) interferograms created by combining 39 synthetic aperture radar (SAR) images to derive the temporal evolution of the line-of-sight (LOS) deformation across the plate boundary and present the deformation accumulated over time of several cross-sections across the rifting plate boundary. By comparing the high-resolution InSAR data to predicted displacements from our GPS-derived steady-state plate-boundary model (Metzger et al., 2013), we test the robustness of the model with a particular focus on the locking depth and slip rate of the HFF. We further identify its weaknesses and improve it by introducing volcanic model parameters to account for transient deformation in the NVZ.

2. Tectonic setting

The TFZ is a result of the relative motion of the North American-Eurasian plate-boundary with respect to the Iceland mantle plume (Morgan, 1983; Lawver and Müller, 1994). The active spreading axis onshore Iceland has had stepwise shifts to the East in order to keep its position above the mantle plume. The last shift in North Iceland took place 6-8.5 Myr ago after the activation of the NVZ, when, as a link to the offshore mid-Atlantic Ridge, the TFZ became active (Sæmundsson, 1979; Homberg et al., 2010). Within the TFZ, the two active lineaments are the HFF, a right-lateral strike-slip fault, and the offshore GOR, which consists of a set of N-S trending normal and strike-slip faults, aligning in a NW-SE direction (Fig. 1). The GOR shows signs of recent volcanic activity (Gudmundsson, 2000; Olafsson et al., 1990; Botz et al., 1999).

The NVZ consists of several central volcanoes and associated fissure swarms (Fig. 1) that accommodate the plate spreading during rifting episodes, which occur every few hundred years, with abrupt widening of several meters. Theistareykir is the western-most fissure swarm of the NVZ (Fig. 1). In 1867-1868, an earthquake sequence that included an estimated magnitude 6 earthquake occurred and was accompanied by volcanic eruptions in the offshore part of the Theistareykir fissure swarm (Thoroddsen, 1925; Halldórsson, 2005; Magnúsdóttir and Brandsdóttir, 2011). The last rifting activity in this episode took place in 1884-1885 and included a M6.3 earthquake (Halldórsson, 2005) and 2 m of subsidence along a 100 m wide N-S striking graben near the coast (Thoroddsen, 1925; Halldórsson, 2005; Magnúsdóttir and Brandsdóttir, 2011). The last unrest of the Theistareykir fissure swarm occurred between 2007 and 2009 when in total $\sim$8 cm of uplift was observed. A point pressure source (Mogi, 1958) with a volume increase of 25×10^6 m^3 at 8.5 km depth was used to model the observations (Metzger et al., 2011, 2013).

The most recent rifting episode in North Iceland occurred within the Krafla volcanic system, east of Theistareykir, from 1975 to 1984. During those nine years, more than 20 intrusive events took place with an average total widening of 5 m, corresponding to $\sim$275 years of plate spreading (Tryggvason, 1980; Björnsson, 1985; Tryggvason, 1984, 1994). A transient deformation pulse, triggered by the rifting episode, propagated away from the rift axis and slowly decayed in amplitude (Foulger et al., 1992; Heki et al., 1993; Hofton and Foulger, 1996). The horizontal plate-boundary deformation rates had returned back to normal by 2000 (Völksen, 2000) or at the latest by 2005 (Árnadóttir et al., 2009). Large-scale uplift was detected north of Krafla central volcano in several interferograms spanning the 1993-1999 time period and modeled with a deep magma source at 21 km depth with a volume change rate of 26×10^6 m^3/yr (de Zeeuw-van Dalfsen et al., 2004). The authors also showed that local subsidence at Krafla since 1989 (Tryggvason, 1994) and along the 1975-1984 lava flows was still ongoing during that period. Using finite element modeling, Pedersen et al. (2009) and Ali et al. (2014) showed that the large-scale uplift north of Krafla can also be explained with post-rifting viscoelastic relaxation. Two other volcanic systems exist east of Krafla, Fremrinámur and Askja, but their central volcanoes are located further South. The most recent rifting activity in the Askja fissure swarm took place in 1874-1875 (Sigurdsson and Sparks, 1978), but the last eruption in Askja was in 1961.

3. GPS data

The GPS data are compiled from fifteen continuously operating stations (CGPS) (Metzger et al., 2011) and 44 campaign GPS markers (Jouanne et al., 2006; Metzger et al., 2013). The North Iceland GPS network covers onshore a 150×100 km^2 area, with the highest GPS station density near the HFF, and includes two permanent stations on Flatey and Grímsey islands (Fig. 1), with the highest point density near the onshore part of the HFF. The westernmost CGPS station is at Siglufjörður and we also include data of the semi-permanent GPS station at Egilsstaðir in East Iceland, about 150 km east of Akureyri. This means that we capture the deformation across the entire plate-boundary zone, which has a width of $\sim$40 km (Fig. 1).

The GPS data contain five years of CGPS data (2006-2010) and campaign GPS points that have been measured 5-10 times between 1997 and 2010 (Jouanne et al., 2006; Metzger et al., 2013). The CGPS data were processed with BERNESE 5.0 software (Dach et al., 2007) and the campaign GPS data were processed both with BERNESE 5.0 and GAMIT-GLOBK V10.4 software (Herring et al., 2010c,a,b). The acquisition parameters, data processing and time-series results are discussed at length in Metzger et al. (2011) and Metzger et al. (2013).

4. InSAR data processing

With its scarce vegetation and (mostly) gentle topography, Iceland is ideal for radar interferometry. In this study, we use the large data archive of the ERS mission that spans an observation period of 17 years, starting in 1992. The 110×100 km-aperture of descending track 281, frame 2267, is centered around the onand part of the HFF and extends across the entire plate-boundary zone in North Iceland. We decided to use data acquired from a descending satellite track as more data were acquired during descending passes and the line-of-sight (LOS) of the descending track is more sensitive to the shear motion near the HFF compared to the ascending track LOS.

From 39 SAR images, we formed 92 interferograms (Fig. 2) using the GAMMA software (Werner et al., 2000), an updated DEM as presented in Metzger et al. (2011) and Delft orbits (Scharroo and Visser, 1998). We then unwrapped the high- and low-frequency content of each interferogram separately and recombined the result (Metzger, 2012). The unwrapped data were manually checked and corrected for unwrapping errors by using loops of interferograms. The resulting interferograms show various signal types, depending on the time span: Interferograms spanning several years show plate-boundary deformation and the volcanic deformation at and near Krafla and Theistareykir central volcanoes, while interferograms spanning short periods mostly exhibit signals due to variations in the atmosphere (Fig. 3).

We used the π-RATE (Poly-Interferogram Rate And Time-series Estimator) software package[1] developed by Biggs et al. (2007), Elliot et al. (2008) and Wang et al. (2009) and produced epoch-by-epoch solutions from the network of interferograms. This allowed us to differentiate between transient volcanic signals and the interseismic plate-boundary deformation signal. The latter could easily be misinterpreted as a ramp caused by inaccurate orbital information and removed during the correction process. We therefore temporarily subtracted a predicted deformation field from all the interferograms before we corrected them for quadratic orbital-ramp (and atmospheric) contributions and added the predicted deformation back in again only before the estimation of the time-series. The predicted steady-state plate-boundary deformation was based on the model in Metzger et al. (2013) that was constrained by GPS data.

After correction for orbital contributions, we used the π-RATE package to generate a Minimum Spanning Tree (Kruskal, 1956) for each pixel set of the whole interferogram network to estimate and remove topographic (Elliot et al., 2008) and atmospheric phase delays (using spatio-temporal filtering, after Hanssen, 2001, and Parsons et al.,

[1] http://homepages.see.leeds.ac.uk/~earhw/software/pi-rate/

2006) and to carry out the final time-series analysis using finite difference smoothing (Schmidt and Bürgmann, 2003). We used a variance-covariance matrix for data weighting to account for correlation between interferograms and presence of noise. The InSAR time-series result showed a slight correlation with topography, which we corrected using the DEM of Metzger et al. (2011).

5. Crustal deformation 1992-2009

As an outcome of the InSAR time-series analysis, we present the average LOS displacement rates between 1992 and 2009 with respect to stable North America (Fig. 4a), meaning that the average deformation rate of pixels to the west of the NVZ is equal to 0, whereas the Eurasian plate, east of the NVZ, is moving towards the satellite at a rate of ∼7 mm/yr, corresponding to ∼18 mm/yr horizontal plate widening rate. A N-S-trending corridor restricted by the Theistareykir fissures to the west and the Krafla fissures in the east moves at an intermediate LOS rate of 3-5 mm/yr (Fig. 4a). Little distinct deformation seems to be associated with the Fremrinámur or the Askja fissure swarms suggesting that – within the extent of the SAR image frame – these fissure swarms currently do not accommodate much of the plate-spreading at this latitude. Across the HFF no sharp rate-change indicative of fault-creep is visible. The data show only a small gradual LOS rate change from the area south of the HFF to the tip of the Tjörnes peninsula. The expected LOS signal difference is only ∼2 mm/yr given the 6.8±0.3 mm/yr fault slip-rate (Metzger et al., 2013), which appears to be close to the detection threshold. The deformation near the HFF is discussed further in section 6.1.

Apart from the plate-motion signal, the four most prominent deformation signals that the time-series results reveal (Fig. 4a) are found within the NVZ: (1) Large-scale uplift, centered ∼20 km NNE of Krafla central volcano, affecting a 30×60 km area and causing average LOS uplift rates of up to 16 mm/yr. (2) A somewhat smaller-scale uplift signal is found slightly east of Theistareykir central volcano, displaying average deformation of ∼9 mm/yr. (3) Strong subsidence occurs locally at Krafla central volcano with LOS deflation rates of 7 to 10 mm/yr. In addition to this signal, we can also outline the 1975-1984 lava flows that came from eruptive fissures near and north of Krafla central volcano in several eruptions, covering an area of 38 km^2 (Tryggvason, 1994). A narrow band of subsidence, just north of Krafla, coincides with the lava flows and is likely caused by cooling and compaction of the flows. Finally, (4) at Krafla, a broad NNE-SSW trending subsidence channel south of the central volcano is visible. This channel aligns with the sharp rate change visible at the eastern edge of Krafla fissure swarm close to the north coast but is stronger, with smoother gradients, and symmetric towards east and west with a rate difference of ∼5 mm/yr.

The InSAR time-series results show that the plate-boundary motion is not entirely uniform across the NVZ, but is focused along different discontinuities. We present LOS displacement profiles across the NVZ at three different latitudes and their evolution through time during the past two decades, in order to show better the current plate boundary deformation (Fig. 4b) and transient volcanic processes. The profiles are located across the Theistareykir, Krafla and Fremrinámur fissure swarms near the north coast (W1-E1, Fig. 4a) and across Theistareykir (W2-E2) and Krafla central volcanoes (W3-E3). Each point on a profile is the average of 40 pixels across the profile (4 km) and 9 pixels along the profile (900 m), and each colored profile line corresponds to one additional year of deformation, averaged from all time-series analysis results of the given year (for the years 1995, 2002 and 2005 that follow a year without SAR acquisitions: Two years of additional deformation). The three profiles all show the plate widening across the NVZ, i.e., the eastern ends of the profile show positive displacement into the line-of-sight. In the discussion below, one needs to keep in mind that the LOS displacements are a combination of this gradual plate widening signal and transient volcanic signals.

a) Plate extension across Krafla, Theistareykir and Fremrinámur fissure swarms

In the NVZ near the coast, we see a sharp rate-change that coincides with the eastern edge of the Krafla fissure swarm with an accumulated LOS offset of 50 mm during 1992-2009 (Fig. 4b, W1-E1, features marked with 1.). This sharp change is visible through the entire delta of the Jökulsá river at Öxafjörður (Fig. 4a). We believe that this discontinuity is evidence of creep occurring on a shallow normal fault along the Krafla fissure swarm. The western border of the Krafla fissure swarm shows accumulated LOS displacement of ∼30 mm in the opposite direction, indicating local subsidence within the fissure swarm (2.). Another discontinuity along this profile corresponds to the western edge of the Fremrinámur fissure swarm (3.) where we see a total of ∼30 mm LOS subsidence. At the western end of Theistareykir fissure swarm (4.), the LOS deformation also increased by ∼25 mm over the observed time period. The negative signal seen in the Askja fissure swarm (5.), resembling a trough, is probably a residual atmospheric signal, as it appears to correlate to the topography, or is related to local slope movements.

b) Uplift at Theistareykir and north of Krafla

Profile W2-E2 crosses the Theistareykir central volcano and the area of maximum uplift northeast of Krafla. Our results show clearly that the broad uplift north of Krafla, first reported by de Zeeuw-van Dalfsen et al. (2004) in 1993-1999 InSAR data, is still ongoing (Fig. 4b, W2-E2). The inflation rate seems to have been rather stable until 2007 and then slowed down slightly.

The observed LOS displacement at Theistareykir is mostly a combination of plate spreading and the broad uplift north of Krafla. But Theistareykir also shows two distinct phases of inflation (marked with arrows) during 1995-1996 (18 mm LOS) and 2006-2009 (78 mm LOS, Metzger et al., 2013) that both extend into the Krafla fissure swarm.

c) Deflation at Krafla central volcano

The profile across Krafla central volcano is dominated by the plate-boundary extension signal and strong subsidence at Krafla with a relative LOS subsidence of $\sim$200 mm during the 17 year-long time-series (Fig. 4b, W3-E3). This subsidence is likely caused by magma cooling/contraction or drainage at the caldera into the lower crust stimulated by plate spreading (de Zeeuw-van Dalfsen et al., 2004, 2006). The subsidence rate slowed down from 50 mm/yr in 1990 (Tryggvason, 1994) to 10 mm/yr in 1997 (Ágústsson, 2001) and decreased further to an average of $\sim$6 mm/yr during 2000-2009.

6. Modeling the plate boundary deformation

6.1. Strain accumulation across the Húsavík-Flatey Fault

One of the main aims of our study is to investigate if the addition of InSAR data can improve the interseismic fault parameter estimation for the HFF. We extracted InSAR time-series analysis results along a profile crossing the HFF after removing the volcanic signals at Theistareykir and Krafla (using the models described in section 6.2b and c), leaving only interseismic deformation (Fig. 5). The profile values show a gradual rate-change across the fault of 2-3 mm/yr, despite the $\pm$1-2 mm/yr scatter of the data points. The median of the InSAR data values along the profile match both the horizontal GPS observations (projected into line-of-sight) and the GPS-derived model prediction well. However, the InSAR results are significantly more noisy than the GPS velocities and also contain more local variations that do not seem to be related to the HFF. We therefore conclude that the inclusion of the InSAR results does not help to improve the estimates of the HFF slip rate and locking depth.

6.2. Towards an enhanced model of the TFZ and NVZ

Thanks to the increased spatial and temporal coverage of the InSAR data, we can now better separate transient volcanic signals from the steady-state plate motion. To test the robustness of our model approach and assess the influence of various types of input data to the model parameters we combine our interseismic, inter-rifting plate-boundary model of Metzger et al. (2011, 2013) with a set of point pressure sources (Mogi, 1958) that represent the relevant deformation processes during the last two decades in the NVZ (see Table 1). The different model contributions are explained in the following paragraphs.

a) Steady-state plate-boundary deformation

The interseismic back-slip model geometry is fixed and consists of nine planar segments in an elastic half-space, describing the plate boundary along the HFF, GOR and NVZ (Table 1, Fig. 6d). Where possible, the segments have been aligned with clear surface features, i.e. along the HFF and the eruptive fissures of the last Krafla rifting episode. At other locations the segments depict a simplification of the complicated tectonics of North Iceland (GOR, KR, NVZ). Rigid block motion combined with back-slip on the upper, locked part of the segments results in modeled interseismic and inter-rifting deformation. All segments are vertical and extend from the surface down to the segment locking depth L_d. The rate across each segment (strike-slip and opening but no dip-slip) is derived from the plate motion rate and azimuth as well as the relative slip partition between the HFF and the GOR segments. The locking depth marks the boundary between the upper, locked and lower, freely slipping fault segments and is twofold, one for all transform-type segments representing the HFF and the GOR, and one for all rift-type segments. For more details about the model set up we refer to Metzger et al. (2011).

b) The Krafla subsidence and broad uplift in the NVZ

At least since 1993 (de Zeeuw-van Dalfsen et al., 2004) but probably since the Krafla rifting episode (Ali et al., 2014), a broad, $30 \times 60\,\mathrm{km}^2$ area slightly north of the Krafla central volcano has been uplifting. Subsidence within the Krafla caldera has been ongoing since 1989. The uplift has been explained by magma accumulation at 21 km depth (de Zeeuw-van Dalfsen et al., 2004; Sturkell et al., 2008), while the shallow source of the Krafla deflation was estimated to be at 2.4 km depth and likely related to magma cooling/contraction (de Zeeuw-van Dalfsen et al., 2004). We follow the approach of de Zeeuw-van Dalfsen et al. (2004) and model both the uplift and the subsidence with Mogi sources. Since this deformation continued after 1999 (see profile W2-E2 in Fig. 4b), we re-estimate the depth and total volume change but keep the reported Mogi locations fixed (Table 1, Fig. 6b).

c) Volcanic deformation at Theistareykir (2007 – 2009)

Theistareykir central volcano experienced two periods of unrest, during 1995-1997 and during 2007-2009 (Metzger et al., 2013). The unrest in 1995-1997 may have been linked to the deep activity north of Krafla described above, and we therefore do not distinguish it from the broad uplift signal mentioned above. The inflation during the second period, on the other hand, has been attributed to an increase in reservoir pressure at 8.5 km depth beneath Theistareykir central volcano (Metzger et al., 2011, 2013). In the model parameter optimizations presented here, we also re-estimate the source depth and volume change but keep the location derived from ascending and descending ENVISAT data by Metzger et al. (2013) (Table 1, Fig. 6b).

d) Post-rifting relaxation of the Krafla rifting episode

Post-rifting relaxation was clearly observed after the Krafla rifting episode (Hofton and Foulger, 1996) and decayed in amplitude with time. We do not include post-rifting relaxation in our modeling, because its influence on the InSAR time-series results is rather limited.

6.3. Data subsampling, modeling method and error estimation

Using the model setup of dislocation segments and Mogi sources described in section 6.2 and in Table 1, we find the best-fit model parameters using a non-linear optimization routine. By varying the input data (GPS/InSAR), we can test the model's robustness and compare the results to the best-fit model parameters obtained from the purely interseismic, steady-state model setup of Metzger et al. (2013).

The data set resulting from the InSAR time-series analysis was reduced to 305 data points using quad-tree subsampling (Jónsson et al., 2002) with varying cell sizes from 0.8 km to 25.6 km. The error of each grid cell is derived empirically using a geo-statistical approach with semi-variograms and co-variograms of a neutral, undeformed area within the InSAR data (Sudhaus and Jónsson, 2008, 2011). We find uncertainties in the range of 0.03-0.2 mm/yr from the largest to the smallest cells. These uncertainties are then directly combined with uncertainties of the GPS data of Metzger et al. (2013), which are in the range 0.2-1.0 mm/yr for the horizontal and 1.0-4.0 mm/yr for the vertical components and used for the data weighting in the modeling. A final model parameter is introduced to correctly position the InSAR data in the North America fixed model reference frame.

The best-fit model parameters are estimated with a two-step optimization routine: During the first step, the model space is initially scanned randomly with a simulated annealing Monte Carlo-type algorithm that, with decreasing "temperature" progressively begins to favor certain parts of the model space that likely have good data fit (Cervelli et al., 2001). The goal is to have the search ending near the *global* minimum of the model space. The second step uses a derivative-based search algorithm that starts the parameter search with the best parameters from the first step and follows the down-dip along the strongest gradient of the model-misfit space until it hits the minimum.

We estimated the model parameter uncertainties empirically by adding synthetic noise to the input data and repeating the optimization routine 500 times. The amplitude of the noise is defined by the data weight, i.e., the inverse of the covariance matrix. Strong correlation is usually observed between the depth and volume of the Mogi sources. Apart from that, only the HFF locking depth and the full plate motion show a slight correlation.

6.4. Comparing models with varying degrees of freedom and amount of input data

We tested different model setups with a varying number of parameter constraints. The set of model results we refer to as A has the plate motion azimuth tightly constrained when InSAR data were used. The model results B and C include amplitude and azimuth constraints for the plate motion: For B, we fixed the plate motion at the outcome of model A-1 (19.9 mm/yr at 111.9°N); for C, we used the plate motion given by the MORVEL plate motion model (18.4 mm/yr at 104.0°N, DeMets et al., 2010). We tested all model setups for the influence on the best-fit parameters when using (numbered with “-1”) the GPS data alone, (“-2”) only InSAR data and (“-3”) both the GPS and InSAR data. In the optimization runs with only the GPS data, we excluded volcanic source parameters representing subsidence at Krafla central volcano due to the low spatial resolution of the GPS data. The outcome of different optimization runs with varying data input and model parameter constraints are listed in Table 2, where they are compared with the earlier interseismic steady-state plate boundary model of Metzger et al. (2013), which we refer to as the *reference* model.

7. Modeling results

7.1. Plate-boundary parameters

First, we updated the original model of Metzger et al. (2013) by adding a Mogi source to represent the broad uplift observed north of Krafla, resulting in model parameter set A-1 (Table 2). We found that the locking depth of the HFF increases somewhat from 6.2 to 8.5 km. By accounting for this large-scale uplift north of Krafla, we could explain some of the (increased) eastward motion of the GPS points by volcanic deformation rather than by interseismic and interrifting deformation (Fig. 6c). This resulted in a slightly decreased plate divergence rate from 20.3 to 19.9 mm/yr at a slightly different azimuth and the deeper locking depth. Generally, the model parameter uncertainties increase, which is probably caused by the higher number of free model parameters.

The surface deformation seen by InSAR is one-dimensional in the line-of-sight. This means that model optimization using only InSAR data cannot well constrain both the amplitude and azimuth of the plate motion. We therefore constrained the plate-spreading azimuth in all optimization runs containing only InSAR data to values derived from the MORVEL plate motion model (DeMets et al., 2010) or our earlier results (Metzger et al., 2013). Given these constraints, when using only InSAR data (model A-2, Table 2), we found a plate-spreading rate of 23.7 mm/yr, which is higher than the 17-19 mm/yr predicted by most of the well-established plate motion models. Further, we found slightly more slip occurring on the HFF (37.8%) than that estimated by Metzger et al. (2013) (33.4%). The locking depth of the ridge segments seems to be positively correlated to the plate spreading for all model runs with values between 3.1 and 5.8 km. Slip on the HFF increases to 38.2% if GPS and InSAR data are combined, and the locking depth parameter increases to 10.2 km, which is the highest value of all the model outcomes (model A-3).

In the model set B we fixed both the plate motion azimuth and rate using the result of model A-1, which was constrained by GPS data alone (Table 2). This led to a very shallow locking depth for the InSAR-only solution of 3.2 km and 30.1% partial motion on the HFF. Using the combined dataset also led to lower values than before (6.8 km, 34.7%). This tendency continued, when we further fixed the plate motion according to the MORVEL plate-motion model (DeMets et al., 2010) at 18.4 mm/yr in a direction of 104.0 °N (model set C, Table 2).

The robustness of and correlation between model parameters are more easily analyzed when using scatter plots. Here, we concentrate on the most important model parameters for the seismic potential of the HFF, i. e., the fault locking depth and the slip rate. The slip rate on the HFF is derived from the portion of the transform motion accommodated by the HFF and the plate divergence rate. There is a clear dependency between the slip rate (or plate divergence) and the locking depth of the HFF with higher slip rates calling for greater locking depths (Fig. 7). The poorest parameter constraints are obtained with the InSAR data alone, where we see a range of 5-9 mm/yr for the slip rate in relation to a wide range of locking depth values of 2 to 7.5 km. The GPS data provide a more stable result with almost no variation in the slip rate and a range of locking depths of 6.2-8.7 km. Apart from the surprising result of model A-3, the best-fit model parameters of the combined data set are found in between the solutions for the individual data sets.

7.2. Volcanic parameters

The volcanic model parameters are less sensitive to a change in the plate divergence rate than are the plate-boundary model parameters, but they are as sensitive with regard to the input data type (Table 2). There are several reasons for this, with the most obvious one being the difference in the time span between the two data sets, with InSAR starting in 1992 and GPS later in 1997. Another reason is that the GPS data alone cannot distinguish well between the two centers of uplift at Theistareykir and northeast of Krafla. If InSAR data are included in the optimization, we find a total volume change of $\sim 350 \times 10^6$ m^3 in 17 years, which is more than twice the volume change of $\sim 150 \times 10^6$ m^3 during 1993-1999 estimated by de Zeeuw-van Dalfsen et al. (2004).

The estimated deflation rate of Krafla central volcano increases with a decreasing plate divergence rate (Table 2). Our plate motion model predicts subsidence along the rifting segments (see Fig. 6d), which increases with an accelerated plate divergence and might account for some of the subsidence at Krafla, similar to the evidence at Askja (de Zeeuw-van Dalfsen et al., 2012). We estimate the source of the subsidence to be slightly deeper (3.7-4.6 km) with a larger volume change rate (0.46-0.76 $\times 10^6$ m^3/yr) than de Zeeuw-van Dalfsen et al. (2004) (2.4 km, 0.3-0.5 $\times 10^6$ m^3/yr).

7.3. Residual deformation

We compare the InSAR time-series results (Fig. 6a) with predicted ground velocities (model B-3, Fig. 6b) to analyze deformation not explained by the model. We first isolate the interseismic and inter-rifting plate boundary deformation by removing all predicted volcanic signals from the observed InSAR data (Fig. 6c). These plate-boundary LOS displacements are mostly due to horizontal ground displacements, except for the subsidence along the Krafla fissure swarm as shown in Fig. 4. However, the plate divergence is not uniform across the plate-boundary zone and seems to be somewhat concentrated on fissures within the Theistareykir and the Krafla fissure swarms and, in the North, along the western margin of Fremrinámur fissure swarm. The interseismic model prediction shown in Fig. 6d fits the InSAR time-series results overall very well with a residual RMS value of only 1.43 mm/yr (Fig. 6e,f). The strongest unmodeled deformation is seen in the vicinity of Krafla central volcano. The residual subsidence north of the Krafla caldera corresponds to the 1975-1984 lava flows but the subsidence south of Krafla central volcano remains unexplained, as no recent lava flow is present there. Within the boundaries of the Krafla central volcano, we see residual local subsidence (Fig. 6f) that is likely related to the Krafla and Bjarnaflag geothermal fields (Spaans et al., 2012).

8. Which model parameter set is the best?

InSAR and GPS data are widely used together to constrain co-seismic fault plane solutions and fault slip parameters (e.g., Feng and Jónsson, 2012; Hayes et al., 2010; Jónsson et al., 2002; Sudhaus and Jónsson, 2008, 2011; Wright et al., 1999) and to assess post-seismic deformation (e.g., Chlieh et al., 2004; D'Agostino et al., 2012; Decriem and Árnadóttir, 2012; Fialko, 2004; Jónsson, 2008) and inter-seismic crustal deformation (e.g., Cavalié and Jónsson, 2014; Gourmelen et al., 2011; Smith and Sandwell, 2006; Wang et al., 2009). Many of these publications have shown that the three-dimensional, absolute information from GPS with low spatial resolution and the one-dimensional, relative line-of-sight information from InSAR data with high spatial resolution complement each other well.

In the work presented here, the addition of InSAR data helped to better discriminate between transient volcanic and steady-state extensional processes. However, it did not improve the HFF model parameter estimation compared to what was derived from GPS data alone. We believe that this is mainly due to the high density of GPS stations near the HFF, which better captured the deformation across the fault, whereas the lack of offshore InSAR data and the complexity of the tectonics in the area contributed to the limited impact of adding the InSAR data. With one exception, the faults examined in the interseismic studies cited above have higher slip rates than the HFF: A LOS deformation rate of $\sim$4 mm/yr was measured across the Haiyuan Fault on the Tibet-Qinghai plateau (Cavalié et al., 2008) as well as across the Denali Fault in Alaska (Biggs et al., 2007). A rate of 7-8 mm/yr was observed at the North Anatolian Fault in Turkey (Walters et al., 2011) and an accumulated LOS deformation rate of $\sim$13 mm/yr was measured across the San Andreas and the San Jacinto Faults in California (Fialko, 2006). In the case of the HFF, we expect a LOS rate change of only $\sim$2 mm/yr (Fig. 5). This relatively small rate change across the fault is difficult to observe with InSAR. Gourmelen et al. (2011) succeeded in detecting a LOS deformation rate of only 1.5 mm/yr across the Hunter Mountain fault, Eastern California, using time-series analysis of 44 ERS SAR scenes and modeled the deformation with 4.9$\pm$0.8 mm/yr slip rate and a shallow locking depth of 2.0$\pm$0.4 km (Gourmelen et al., 2011). In all these studies, the faults extend across the whole or most of the SAR image frame, whereas only a fifth of the HFF is covered by SAR data, because most of the fault is offshore (Fig. 1). Therefore, we can only examine the eastern end of the transform fault.

It is somewhat surprising that the best-fit locking depth and motion partition, using the combined input data set A-3, are not between the results obtained from using the two geodetic datasets separately. The influence of the InSAR data on the locking depth parameter of the HFF also shows that the small parameter uncertainty reported in our earlier work was too optimistic, as we already had stated (Metzger et al., 2013), and that the locking depth might be deeper than previously estimated. The solution of model A-3 also has a rather high spreading rate of 22.2 mm/yr, which is well above all predictions from standard global plate-motion models that are in the range of 16.5-19.5 mm/yr.

We therefore conclude that the locking-depth is between 6-10 km and that it may be varying along the fault, due to the decreasing thermal gradient away from the NVZ (Flóvenz and Sæmundsson, 1993; Metzger et al., 2013). We further confine the slip rate to be in the range of 6-9 mm/yr, with 34-37% of the transform motion accommodated by the HFF. If we assume a full stress release during the last two large earthquakes in 1872 and a steady accumulation of slip-deficit since then, we find that it is equivalent to a moment magnitude M_w6.8-7.0 earthquake, given an instantaneous rupture of the entire HFF. This estimation is somewhat larger than what we estimated from the GPS-only model (M_w6.8$\pm$0.1, Metzger et al., 2013). However, the influence of the Krafla rifting episode should not be ignored. Recent Coulomb failure stress change (ΔCFS) modeling of the rifting episode suggests that the ΔCFS was negative on the eastern end of the HFF, indicating that this part of the fault was pushed further away from failure by the rifting activity (Maccaferri et al., 2013). This may also explain the lack of micro-seismicity near Húsavík (Fig. 1).

9. Conclusions

InSAR time-series analysis of 17 years of ERS data covering the plate-boundary zone in North Iceland shows a ~40-km wide deforming corridor along the Northern Volcanic Zone with most of the deformation occurring within the Krafla and Theistareykir volcanic systems. Thanks to the high resolution in space and time, the InSAR data provide information about inflation at Theistareykir (1995-1997, 2007-2009), broad uplift north of Krafla (since 1993, now slightly decelerating) and subsidence at Krafla central volcano (decaying since the Krafla rifting episode). On the other hand, the LOS rate-change across the HFF is hardly detectable.

We describe the ongoing plate boundary deformation using an interseismic back-slip model of dislocation segments combined with point pressure sources to estimate the locking depth and slip rate of the HFF. Various optimization runs show that the best-fit model parameters as well as the parameter uncertainty range depend on the type of input data (GPS, InSAR), the number of model parameters and the parameter constraints. We find a correlation between the slip rate and locking depth of the HFF, with larger locking depths found at larger slip rates. We show that InSAR data alone are not able to constrain the plate-boundary model parameters well. The model parameter estimations of different combinations of input data show that the HFF accommodates one third of the full transform motion, which is equivalent to a slip rate of 6-9 mm/yr, and that it has a locking depth of 6-10 km.

10. Acknowledgments

ERS data were provided by the European Space Agency through category-1 project #3846. We thank Matthew Garthwaite for a detailed explanation of the π-RATE code and Henriette Sudhaus for assistance with the uncertainty estimation of the InSAR data. Figure 1 was produced with the GMT public domain software (Wessel and Smith, 1998). We also thank the two reviewers and the editor for helpful comments on the manuscript. The research reported in this publication was supported by GFZ Potsdam, ETH Zürich and King Abdullah University of Science and Technology (KAUST).

References

Ágústsson, S.M., 2001. Ground elevation changes at Krafla: Elevation measurements in 2000 and comparison to the measurements made in 1995 (in Icelandic). University of Iceland, Reykjavík , 30pp.

Ali, S.T., Feigl, K.L., Carr, B.B., Masterlark, T., Sigmundsson, F., 2014. Geodetic measurements and numerical models of rifting in Northern Iceland for 1993–2008. Geophys. J. Int. 196, 1267–1280. doi:doi:10.1093/gji/ggt462.

Árnadóttir, T., Jiang, W., Feigl, K.L., Geirsson, H., Sturkell, E., 2006. Kinematic models of plate boundary deformation in southwest Iceland derived from GPS observations. J. Geophys. Res. 111. doi:10.1029/2005JB003907.

Árnadóttir, T., Lund, B., Jiang, W., Geirsson, H., Björnsson, H., Einarsson, P., Sigurdsson, T., 2009. Glacial rebound and plate spreading: results from the first countrywide GPS observations in Iceland. Geophys. J. Int. 177, 691–716. doi:10.1111/j.1365-246X.2008.04059.x.

Biggs, J., Wright, T., Lu, Z., Parsons, B., 2007. Multi-interferogram method for measuring interseismic deformation: Denali Fault, Alaska. Geophys. J. Int. 170, 1165–1179. doi:10.1111/j.1365-246X.2007.03415.x.

Björnsson, A., 1985. Dynamics of crustal rifting in NE Iceland. J. Geophys. Res. 90, 151–162.

Böðvarsson, R., Rögnvaldsson, S.T., Jakobsdóttir, S.S., Slunga, R., Stefánsson, R., 1996. The SIL data acquisition and monitoring system. Seismol. Res. Lett. 67, 35–46.

Böðvarsson, R., Rögnvaldsson, S.T., Slunga, R., Kjartansson, E., 1999. The SIL data acquisition system – at present and beyond year 2000. Phys. Earth Planet. Inter. 113, 89–101. doi:10.1016/S0031-9201(99)00032-1.

Botz, R., Winckler, G., Bayer, R., Schmitt, M., Schmidt, M., Garbe-Schönberg, D., Stoffers, P., Kristjansson, J.K., 1999. Origin of trace gases in submarine hydrothermal vents of the Kolbeinsey Ridge. Earth Planet. Sci. Lett. 171, 83–93. doi:10.1016/S0012-821X(99)00128-4.

Cavalié, O., Jónsson, S., 2014. Block-like plate movements in eastern Anatolia. Geophys. Res. Lett. 41, 1–6. doi:10.1002/2013GL058170.

Cavalié, O., Lasserre, C., Doin, M.P., Peltzer, G., Sun, J., Xu, X., Shen, Z.K., 2008. Measurement of interseismic strain across the Haiyuan fault (Gansu, China), by InSAR. Earth Planet. Sci. Lett. 275, 246–257. doi:10.1016/j.epsl.2008.07.057.

Cervelli, P., Murray, M.H., Segall, P., Aoki, Y., Kato, T., 2001. Estimating source parameters from deformation data, with an application to the March 1997 earthquake swarm off the Izu Peninsula, Japan. J. Geophys. Res. 106, 11217–11237. doi:10.1029/2000JB900399.

Chlieh, M., de Chabalier, J.B., Ruegg, J.C., Armijo, R., Dmowska, R., Campos, J., Feigl, K.L., 2004. Crustal deformation and fault slip during the seismic cycle in the North Chile subduction zone, from GPS and InSAR observations. Geophys. J. Int. 158, 695–711. doi:10.1111/j.1365-246X.2004.02326.x.

Dach, R., Hugentobler, U., Fridez, P., Meindl, M., 2007. Bernese GPS Software Version 5.0. Stämpfli Publications AG, Bern.

D'Agostino, N., Cheloni, D., Fornaro, G., Giuliani, R., Reale, D., 2012. Space-time distribution of afterslip following the 2009 L'Aquila earthquake. J. Geophys. Res. 117. doi:10.1029/2011JB008523.

de Zeeuw-van Dalfsen, E., Pedersen, R., Hooper, A., Sigmundsson, F., 2012. Subsidence of Askja caldera 2000-2009: Modelling of deformation processes at an extensional plate boundary, constrained by time series InSAR analysis. J. Volc. and Geoth. Res. 213-214, 72–82. doi:10.1016/j.jvolgeores.2011.11.004.

de Zeeuw-van Dalfsen, E., Pedersen, R., Sigmundsson, F., Pagli, C., 2004. Satellite radar interferometry 1993–1999 suggests deep accumulation of magma near the crust-mantle boundary at the Krafla volcanic system, Iceland. Geophys. Res. Lett. 31, 5–9. doi:10.1029/20004GL020059.

de Zeeuw-van Dalfsen, E., Rymer, H., Williams-Jones, G., Sturkell, E., Sigmundsson, F., 2006. Integration of micro-gravity and geodetic data to constrain shallow system mass changes at Krafla Volcano, N Iceland. Bull. Volc. 68, 420–431. doi:10.1007/s00445-005-0018-5.

Decriem, J., Árnadóttir, T., 2012. Transient crustal deformation in the South Iceland Seismic Zone observed by GPS and InSAR during 2000-2008. Tectonophys. 581, 6–18. doi:10.1019/j.tecto.2011.09.028.

DeMets, C., Gordon, R.G., Argus, D.F., 2010. Geologically current plate motions. Geophys. J. Int. 181, 1–80. doi:10.1111/j.1365-246X.2009.04491.x.

Einarsson, P., 2008. Plate boundaries, rifts and transforms in Iceland. Jökull 58, 35–58.

Elliot, J.R., Biggs, J., Parsons, B., Wright, T.J., 2008. InSAR slip rate determination on the Altyn Tagh Fault, northern Tibet, in the presence of topographically correlated atmospheric delays. Geophys. Res. Lett. 35(L12309). doi:10.1029/2008GL033659.

Feng, G.C., Jónsson, S., 2012. Shortcomings of InSAR for Studying Megathrust Earthquakes: The case of the M_w9.0 Tohoku-Oki Earthquake. Geophys. Res. Lett. 39, 6–11. doi:10.1029/2012GL051628.

Fialko, Y., 2004. Evidence of fluid-filled upper crust from observations of postseismic deformation due to the 1992 Mw7.3 Landers earthquake. J. Geophys. Res. 109, B08401. doi:10.1029/2004JB002985.

Fialko, Y., 2006. Interseismic strain accumulation and the earthquake potential on the southern San Andreas fault system. Nature 441, 968–971. doi:10.1038/nature04797.

Flóvenz, Ó.G., Sæmundsson, K., 1993. Heat flow and geothermal processes in Iceland. Tectonophysics 225, 123–138.

Foulger, G.R., Jahn, C.H., Seeber, G., Einarsson, P., Julian, B.R., Heki, K., 1992. Post-rifting stress-relaxation at the divergent plate boundary in Northeast Iceland. Nature 358, 488–490.

Geirsson, H., LaFemina, P., Árnadóttir, T., Sturkell, E., Sigmundsson, F., Travis, M., Schmidt, P., Lund, B., Hreinsdóttir, S., Bennet, R., 2012. Volcano deformation at active plate boundaries: Deep magma accumulation at Hekla volcano and plate boundary deformation in south Iceland. J. Geophys. Res. 117. doi:10.1029/2012JB009400.

Gourmelen, N., Dixon, T.H., Amelung, F., Schmalzle, G., 2011. Acceleration and evolution of faults: An example from the Hunter Mountain-Panamint Valley fault zone, Eastern California. Earth Planet. Sci. Lett. 301, 337–344. doi:doi:10.1016/j.epsl.2010.11.016.

Gudmundsson, A., 2000. Dynamics of volcanic systems in Iceland. Annu. Rev. Earth Planet. Sci. 28, 107–140. doi:10.1146/annurev.earth.28.1.107.

Halldórsson, P., 2005. Earthquake activity in N-Iceland (in Icelandic). Icelandic Meteorological Office, report 05021 , p. 34–41.

Hanssen, R.F., 2001. Radar interferometry - Data interpretation and error analysis. Kluwer Academic Publishers.

Hayes, G.P., Briggs, R.W., Sladen, A., Fielding, E.J., Prentice, C., Hudnut, K., Mann, P., Taylor, F.W., Crone, A.J., Gold, R., Ito, T., Simons, M., 2010. Complex rupture during the 12 January 2010 Haiti earthquake. Nature Geosc. 3, 800–805. doi:10.1038/NGEO977.

Heki, K., Foulger, G.R., Julian, B.R., Jahn, C.H., 1993. Plate dynamics near divergent boundaries - geophysical implications of postrifting crustal deformation in NE Iceland. J. Geophys. Res. 98, 14279–14297.

Herring, T.A., King, R.W., McClusky, S.C., 2010a. GAMIT Reference Manual - GPS Analysis at MIT, Release 10.4. Department of Earth, Atmospheric, and Planetary Sciences, Massachusetts Institute of Technology .

Herring, T.A., King, R.W., McClusky, S.C., 2010b. GLOBK Reference Manual - Global Kalman filter VLBI and GPS analysis program, Release 10.4. Department of Earth, Atmospheric, and Planetary Sciences, Massachusetts Institute of Technology .

Herring, T.A., King, R.W., McClusky, S.C., 2010c. Introduction to GAMIT/GLOBK, Release 10.4. Department of Earth, Atmospheric, and Planetary Sciences, Massachusetts Institute of Technology .

Hjartardóttir, A.R., Einarsson, P., Magnúsdóttir, S., Björnsdóttir, T., Brandsdóttir, B., 2013 in press. Fracture systems of the Northern Volcanic Rift Zone, Iceland - an onshore part of the Mid-Atlantic plate boundary. Geological Society, London, Special Publications .

Hofton, M.A., Foulger, G.R., 1996. Postrifting anelastic deformation around the spreading plate boundary, North Iceland. 1. Modeling of the 1987-1992 deformation field using a viscoelastic earth structure. J. Geophys. Res. 101, 25403–25421.

Homberg, C., Bergerat, F., Angelier, J., Garcia, S., 2010. Fault interaction and stresses along broad oceanic transform zone: Tjörnes Fracture Zone, north Iceland. Tectonics 29. doi:10.1029/2008TC002415.

Jóhannesson, H., Sæmundsson, K., 2009. Geological Map of Iceland 1 : 600 000. Tectonics (rev. edn.), Icelandic Institute of Natural History, Reykjavik.

Jónsson, S., 2008. Importance of post-seismic viscous relaxation in southern Iceland. Nature Geosc. 1, 136–139. doi:10.1038/ngeo105.

Jónsson, S., Zebker, H., Segall, P., Amelung, F., 2002. Fault slip distribution of the 1999 M_w 7.1 Hector Mine, California, earthquake, estimated from satellite radar and GPS measurements. Bull. Seismol. Soc. Am. 92, 1377–1389. doi:10.1785/0120000922.

Jouanne, F., Villemin, T., Berger, A., Henriot, O., 2006. Rift-transform junction in North Iceland: rigid blocks and narrow accommodation zones revealed by GPS 1997-1999-2002. Geophys. J. Int. 167, 1439–1446. doi:10.1111/j.1365-246X.2006.03107.x.

Kruskal, J.B., 1956. On the shortest spanning subtree of a graph and the traveling salesman problem. Proc. Am. Math. Soc. 7, 48–50.

LaFemina, P., Dixon, T.H., Malservisi, R., Árnadóttir, T., Sturkell, E., Sigmundsson, F., Einarsson, P., 2005. Geodetic GPS measurements in south Iceland: Strain accumulation and partitioning in a propagating ridge system. J. Geophys. Res. 110. doi:10.1029/2005JB003675.

Lawver, L., Müller, R.D., 1994. Iceland hotspot track. Geology 22, 311–314.

Maccaferri, F., Rivalta, E., Passarelli, L., Jónsson, S., 2013. The stress shadow induced by the 1975-1984 Krafla rifting episode. J. Geophys. Res. 118, 1109–1121. doi:10.1002/jgrb.50134.

Magnúsdóttir, S., Brandsdóttir, B., 2011. Tectonics of the Þeistareykir fissure swarm. Jökull 61, 65–79.

McMaster, R.L., Schilling, J.G.E., Pinet, P.R., 1977. Plate boundary within Tjörnes Fracture Zone on northern Icelands insular margin. Nature 269, 663–668.

Metzger, S., 2012. Seismic potential of the Húsavík-Flatey fault and kinematics of the Tjörnes Fracture Zone, North Iceland, studied using InSAR and GPS. Ph.D. thesis Nr. 20441, ETH Zürich. doi:10.3929/ethz-a-007580688.

Metzger, S., Jónsson, S., Danielsen, G.J.K., Hreinsdottir, S., Jouanne, F., Villemin, T., 2013. The present kinematics of the Tjörnes Fracture Zone, North Iceland, from campaign and continuous GPS measurements. Geophys. J. Int. 192, 441–455. doi:10.1093/gji/ggs032.

Metzger, S., Jónsson, S., Geirsson, H., 2011. Locking depth and slip-rate of the Húsavík Flatey fault, North Iceland, derived from continuous GPS data 2006-2010. Geophys. J. Int. 187, 564–576. doi:10.1111/j.1365-246X.2011.05176.x.

Michalczewska, K., Hreinsdottir, S., Hjartardottir, A.R., Valsson, G., Bennet, R.A., Jonsson, S., 2013. The Iceland ITRF2008 stable North American reference frame, Abstract G13B-0954, presented at Fall Meeting AGU, San Francisco, Calif. .

Mogi, K., 1958. Relations between the Eruptions of Various Volcanoes and the Deformations of the Ground Surfaces around them. Bull. Earthquake Res. Inst., Univ. Tokyo 36, 99–134.

Morgan, W.J., 1983. Hotspot tracks and the early rifting of the Atlantic. Tectonophysics 94, 123–139.

Olafsson, J., Thors, K., Stefansson, U., Jakobsson, S.P., Jenkings, W.J., Thompson, G., Honjo, S., Manheim, F.T., Commeau, R.F., Jones, R.R., 1990. Geochemical observations from a boiling hydrothermal site on the Kolbeinsey Ridge. EOS Trans. AGU 71, 1650.

Parsons, P., Wright, T., Rowe, P., Andrews, J., Jackson, J., Walker, R., Khatib, M., Talebian, M., Bergman, E., Engdahl, E.R., 2006. The 1994 Sefidabeh (eastern Iran) earthquakes revisited: New evidence from satellite radar interferometry and carbonate dating about the growth of an active fold above a blind thrust fault. Geophys. J. Int. 164, 202–217. doi:10.1111/j.1365-246X.2005.02655.x.

Pedersen, R., Sigmundsson, F., Masterlark, T., 2009. Rheologic controls on inter-rifting deformation of the Northern Volcanic Zone, Iceland. Earth Planet. Sci. Lett. 281, 14–26. doi:10.1016/j.epsl.2009.02.003.

Rögnvaldsson, S.T., Gudmundsson, A., Slunga, R., 1998. Seismotectonic analysis of the Tjörnes Fracture Zone, an active transform fault in north Iceland. J. Geophys. Res. 103, 30117–30129. doi:10.1029/98JB02789.

Sæmundsson, K., 1979. Outline of the geology of Iceland. Jökull 29, 7–28.

Sæmundsson, K., Hjartarson, A., Kaldal, I., Sigurgeirsson, M.A., Kristinsson, S.G., Víkingsson, S., 2012. Geological Map of the Northern Volcanic Zone, Iceland. Northern Part. 1 : 100 000. Reykjavík: Iceland GeoSurvey and Landsvirkjun .

Scharroo, R., Visser, P., 1998. Precise orbit determination and gravity field improvement for the ERS satellites. J. Geophys. Res. 103, 8113–8127. doi:10.1029/97JC03179.

Schmidt, D.A., Bürgmann, R., 2003. Time-dependent land uplift and subsidence in the Santa Clara valley, California, from a large interferometric synthetic aperture radar data set. J. Geophys. Res. 108, 2416. doi:10.1029/2002JB002267.

Sigmundsson, F., Vadon, H., Massonnet, D., 1997. Readjustment of the Krafla spreading segment to crustal rifting measured by Satellite Radar Interferometry. Geophys. Res. Lett. 24, 1843–1846. doi:10.1029/97GL01934.

Sigurdsson, H., Sparks, R.S.J., 1978. Rifting episode in North Iceland in 1874-1875 and the eruptions of Askja and Sveinagja. Bull. Volcanol. 41, 149–167.

Smith, B.R., Sandwell, D.T., 2006. A model of the earthquake cycle along the San Andreas Fault System for the past 1000 years. J. Geophys. Res 111. doi:10.1029/2005JB003703.

Spaans, K.H., Sigmundsson, F., Hreinsdóttir, S., Ófeigsson, B.G., 2012. High resolution surface deformation measurements in Iceland's Northern Volcanic Zone: Unraveling multiple deformation sources using InSAR and GPS, Geophysical Research Abstracts, Vol. 14, EGU2012-10604, EGU General Assembly 2012 .

Sturkell, E., Sigmundsson, F., Geirsson, H., Ólafsson, H., Theodórsson, T., 2008. Multiple volcano deformation sources in a post-rifting period: 1989–2005 behaviour of Krafla, Iceland constrained by levelling, tilt and GPS observations. J. Volcanol. Geotherm. Res. 177, 405–417. doi:10.1016/j.jvolgeores.2008.06.013.

Sudhaus, H., Jónsson, S., 2008. Improved source modelling through combined use of InSAR and GPS under consideration of correlated data errors: application to the June 2000 Kleifarvatn earthquake, Iceland. Geophys. J. Int. 176, 389–404. doi:10.1111/j.1365-246X.2008.03989.x.

Sudhaus, H., Jónsson, S., 2011. Source model for the 1997 Zirkuh earthquake (MW= 7.2) in Iran derived from JERS and ERS InSAR observations. Geophys. J. Int. 185, 676–692. doi:10.1111/j.1365-246X.2011.04973.x.

Thoroddsen, T., 1925. Die Geschichte der isländischen Vulkane. D. Kgl. Danske Vidensk. Selsk. Skrifter, Naturwidensk. og Mathem. Afd. 8, 1–458.

Tryggvason, E., 1980. Subsidence events in the Krafla area, North-Iceland, 1975-1979. J. Geophys. 47, 141–153.

Tryggvason, E., 1984. Widening of the Krafla fissure swarm during the 1975-1981 volcano-tectonic episode. Bull. Volc. 47, 47–69.

Tryggvason, E., 1994. Surface deformation at the Krafla volcano, North Iceland, 1982-1992. Bull. Volc. 56, 98–107.

Völksen, C., 2000. Die Nutzung von GPS für die Deformationsanalyse in regionalen Netzen am Beispiel Islands - The use of GPS for deformation analysis in regional networks using the example of Iceland (in German available only). Ph.D. thesis, University of Hannover. p. 103.

Walters, R.J., Holley, R.J., Parsons, B., Wright, T.J., 2011. Interseismic strain accumulation across the North Anatolian Fault from Envisat InSAR measurements. Geophys. Res. Lett. 38. doi:10.1029/2010GL046443.

Wang, H., Wright, T.J., Biggs, J., 2009. Interseismic slip rate of the northwestern Zianshuihe fault from InSAR data. Geophys. Res. Lett. 36. doi:10.1029/2008GL036560.

Werner, C., Wegmüller, U., Strozzi, T., Wiesmann, A., 2000. GAMMA SAR and Interferometric Processing Software. ERS - ENVISAT Symposium, Gothenburg, Sweden, 16-20 October , GAMMA Remote Sensing Research and Consulting AG, Gümligen, Switzerland, URL: http://www.gamma-rs.ch.

Wessel, P., Smith, H.F., 1998. New improved version of the Generic Mapping Tools released. EOS Trans. Am. Geophys. Un. 79, 579. doi:10.1029/98EO00426.

Wright, T.J., Parsons, B.E., Jackson, J.A., Haynes, M., Fielding, E.J., England, P.C., Clarke, P.J., 1999. Source parameters of the 1 October 1995 Dinar (Turkey) earthquake from SAR interferometry and seismic bodywave modelling. Earth and Planetary Sci. Lett. 172, 23–37. doi:10.1016/S0012-821X(99)00186-7.

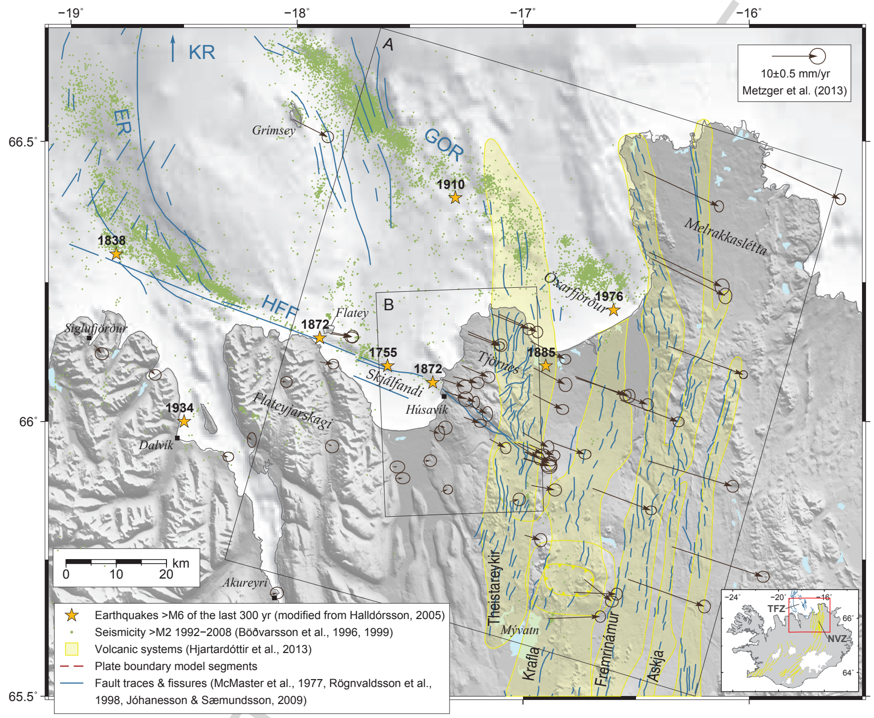

Figure 1: Tectonic setting, earthquake locations and GPS velocities in northeastern Iceland. The Húsavík-Flatey Fault (HFF) links to the Eyjafjarðaráll Rift (ER) and the Kolbeinsey ridge (KR) in the Northwest and, together with the Grímsey Oblique Rift (GOR), to the Northern Volcanic Zone (NVZ) in the Southeast with its fissure swarms and central volcanoes (light yellow). Frame A marks the ERS satellite frame 2267 of track 281 and frame B the area covered in Figure 5. GPS velocities are shown with 95% confidence ellipses and relative to stable North America (MORVEL, DeMets et al., 2010), corrected for a small reference frame shift affecting all stations in northwestern Iceland (Michalczewska et al., 2013).

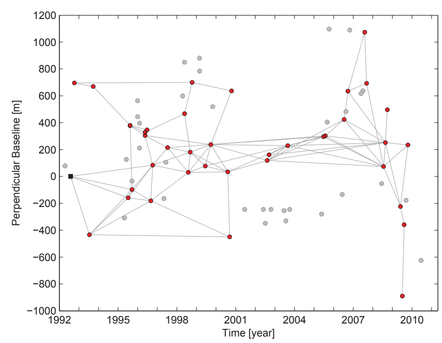

Figure 2: Timeline-baseline plot showing the SAR master scene (black) and the interferogram network generated by combining a number of ERS SAR images (red). The gray dots correspond to unused SAR scenes that resulted in no or low interferometric correlation.

Table 1: Segment location and geometry of the interseismic back-slip model and Mogi model locations (of de Zeeuw-van Dalfsen et al. 2004, if marked with a star, otherwise of Metzger et al. 2013) representing volcanic deformation 1992-2009 (see also Fig. 6b and d). The locking depth parameters (L_d, above L_d segments are locked, below L_d they can slip freely) are reduced to only two values, depending on the segment type. To fulfill half-space conditions, the N-S extension of the ridge segments 5. and 9. are more than ten times larger than the lateral extension of the TFZ. The map projection is UTM-28W, lengths are in kilometers and the strike in degrees and clockwise from North. See Fig. 1 and Fig. 6b for abbreviations.

Segment #	Boundary	Easting	Northing	Length	L_d-type	Dip	Strike
1.	HFF	361.62	7342.93	71.3	transform	90°	116.3°
2.	HFF	407.50	7317.60	33.7	transform	90°	124.4°
3.	GOR	395.95	7371.85	81.7	transform	90°	126.1°
4.	NVZ	425.19	7327.91	40.4	ridge	90°	10.8°
5.	NVZ	347.03	6984.44	664.1	ridge	90°	12.9°
6.	ER	328.44	7375.54	33.8	ridge	90°	175.9°
7.	KR	334.41	7419.87	56.8	ridge	90°	14.6°
8.	KR	352.25	7421.66	55.7	ridge	90°	157.4°
9.	KR	420.79	7774.04	672.2	ridge	90°	13.6°
	Mogi sources				infl./defl.		
K1*	Krafla	418.33	7290.04		deflation		
K2*	Krafla	420.96	7302.24		inflation		
T	Theistareykir	408.50	7309.00		inflation		

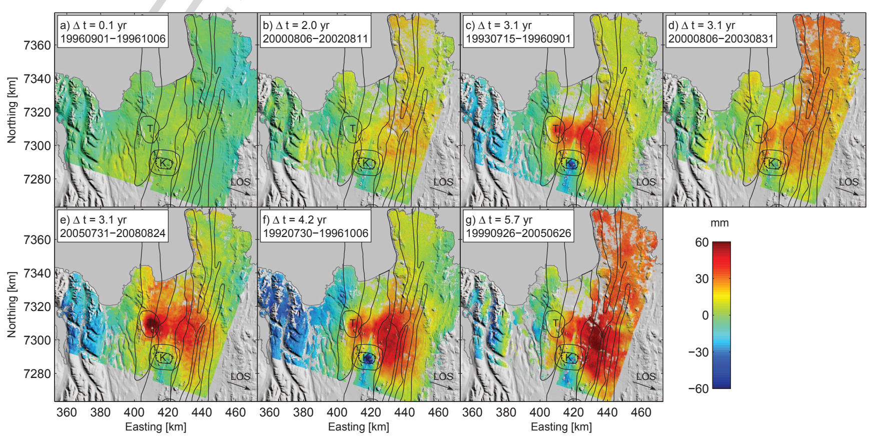

Figure 3: A selection of unwrapped interferograms with different signal types, depending on the temporal baseline (indicated in each panel): Atmospheric delay are the most notable signals in short-period interferograms (e.g. panels a and b), while long-period interferograms are dominated by plate-motion signals (best visible in b, d, and g), broad uplift north of Krafla (K, panels c and e-g) and subsidence within the Krafla caldera (c and f). Uplift at Theistareykir (T) central volcano ocurred between 2007 and 2009 (panel e). Line-of-sight (LOS) directions from the ground towards the satellite are indicated with arrows.

Table 2: Best-fit model parameter and parameter uncertainties for various combinations of input data in comparison to the reference model of Metzger et al. (2013), where, due to data resolution, only deformation at Theistareykir was accounted for. Parameter constraints (in *gray*) for the plate motion rate and azimuth (clockwise from North) are derived from model A-1 (for the models A and B) or the MORVEL plate motion model (18.4 mm/yr, 109.3°N, DeMets et al., 2010, for model C). Unrealistic optimization results with negative values were rejected. The Mogi volume changes are given as rates and absolute numbers multiplied by the length of the GPS (13 yr) and InSAR (17 yr) time-series.

Model set - number	Reference	A-1	A-2	A-3	B-2	B-3	C-1	C-2	C-3
Input data	GPS	GPS	InSAR	GPS/InSAR	InSAR	GPS/InSAR	GPS	InSAR	GPS/InSAR
Rejected models [%]	0	0	3	6	5	5	0	18	5
RMS of InSAR residuals [mm/yr]			1.38	1.43	1.47	1.49		1.51	1.53
Locking depth L_d HFF [km]	$6.2^{+0.8}_{-0.7}$	$8.5^{+1.8}_{-1.4}$	$7.5^{+1.9}_{-2.1}$	$10.2^{+1.3}_{-1.2}$	$3.2^{+1.1}_{-0.8}$	$6.8^{+0.6}_{-0.6}$	$8.7^{+1.2}_{-0.9}$	$2.0^{+1.0}_{-0.6}$	$6.3^{+0.7}_{-0.7}$
Locking depth L_d ridge [km]	$3.2^{+0.2}_{-0.2}$	$4.5^{+0.3}_{-0.3}$	$5.8^{+0.2}_{-0.3}$	$5.6^{+0.2}_{-0.2}$	$4.9^{+0.2}_{-0.2}$	$5.0^{+0.2}_{-0.2}$	$3.1^{+0.2}_{-0.2}$	$4.5^{+0.2}_{-0.2}$	$4.5^{+0.2}_{-0.2}$
Plate spreading [mm/yr]	$20.3^{+0.4}_{-0.3}$	$19.9^{+0.6}_{-0.5}$	$23.7^{+0.7}_{-0.7}$	$22.2^{+0.5}_{-0.4}$	*19.9*	*19.9*	*18.4*	*18.4*	*18.4*
Plate azimuth [°N]	$109.4^{+0.7}_{-0.7}$	$111.9^{+1.0}_{-1.1}$	*111.9*	*111.9*	*111.9*	*111.9*	*104.0*	*104.0*	*104.0*
Partial motion HFF [%]	$33.4^{+1.4}_{-1.4}$	$35.7^{+1.6}_{-1.7}$	$37.8^{+3.7}_{-4.3}$	$38.2^{+2.2}_{-2.3}$	$30.1^{+3.8}_{-3.1}$	$34.7^{+1.9}_{-2.1}$	$37.1^{+1.7}_{-2.1}$	$27.0^{+4.3}_{-3.3}$	$34.0^{+2.1}_{-2.2}$
Source depth K1 (defl.) [km]			$3.7^{+0.2}_{-0.2}$	$3.8^{+0.3}_{-0.2}$	$4.3^{+0.3}_{-0.3}$	$4.1^{+0.2}_{-0.3}$		$4.6^{+0.4}_{-0.3}$	$4.4^{+0.4}_{-0.3}$
Source depth K2 (infl.) [km]		$26.3^{+0.25}_{-0.25}$	$20.7^{+0.7}_{-0.8}$	$21.4^{+0.8}_{-0.7}$	$21.0^{+0.8}_{-0.7}$	$21.2^{+0.7}_{-1.0}$	$25.6^{4.4}_{4.7}$	$21.3^{+0.9}_{-0.7}$	$21.5^{+0.8}_{-0.7}$
Source depth T (infl.) [km]	*8.5*	$8.6^{+1.4}_{-1.5}$	$4.5^{+1.1}_{-0.8}$	$4.0^{+0.8}_{-0.6}$	$3.9^{+0.7}_{-0.6}$	$3.8^{+0.6}_{-1.0}$	$11.9^{+1.5}_{-1.6}$	$3.6^{+0.7}_{-0.6}$	$3.9^{+0.8}_{-0.6}$
Volume change rate K1 [$10^6 m^3$/yr]			$0.46^{+0.09}_{-0.07}$	$0.49^{+0.09}_{-0.08}$	$0.64^{+0.12}_{-0.10}$	$0.59^{+0.10}_{-0.10}$		$0.76^{+0.15}_{-0.10}$	$0.69^{+0.14}_{-0.10}$
Volume change rate K2 [$10^6 m^3$/yr]		$15.6^{+3.2}_{-3.3}$	$21.0^{+1.3}_{-1.5}$	$20.6^{+1.3}_{-1.3}$	$20.3^{+1.4}_{-1.3}$	$20.3^{+1.2}_{-1.4}$	$8.8^{+4.1}_{-3.3}$	$20.5^{+1.3}_{-1.2}$	$20.3^{+1.5}_{-1.2}$
Volume change rate T [$10^6 m^3$/yr]		$1.58^{+0.54}_{-0.43}$	$0.30^{+0.18}_{-0.10}$	$0.25^{+0.11}_{-0.07}$	$0.24^{+0.12}_{-0.07}$	$0.24^{+0.09}_{-0.08}$	$3.69^{+1.05}_{-0.84}$	$0.21^{+0.09}_{-0.07}$	$0.25^{+0.11}_{-0.07}$
Abs. volume change K1 [$10^6 m^3$]			$7.9^{+1.5}_{-1.2}$	$8.4^{+1.5}_{-1.4}$	$11.0^{+2.1}_{-1.7}$	$10.1^{+1.7}_{-1.7}$		$13.1^{+2.6}_{-1.7}$	$11.9^{+2.4}_{-1.7}$
Abs. volume change K2 [$10^6 m^3$]		203^{+42}_{-43}	361^{+22}_{-26}	354^{+22}_{-22}	349^{+24}_{-22}	349^{+21}_{-24}	114^{+53}_{-43}	353^{+22}_{-21}	349^{+53}_{-21}
Abs. volume change T [$10^6 m^3$]	*25*	$20.5^{+7.2}_{-5.6}$	$5.2^{+3.1}_{-1.7}$	$4.3^{+1.9}_{-1.2}$	$4.1^{+2.1}_{-1.2}$	$4.1^{+1.5}_{-1.4}$	$48.0^{+13.7}_{-10.9}$	$3.6^{+1.5}_{-1.2}$	$4.3^{+1.9}_{-1.2}$

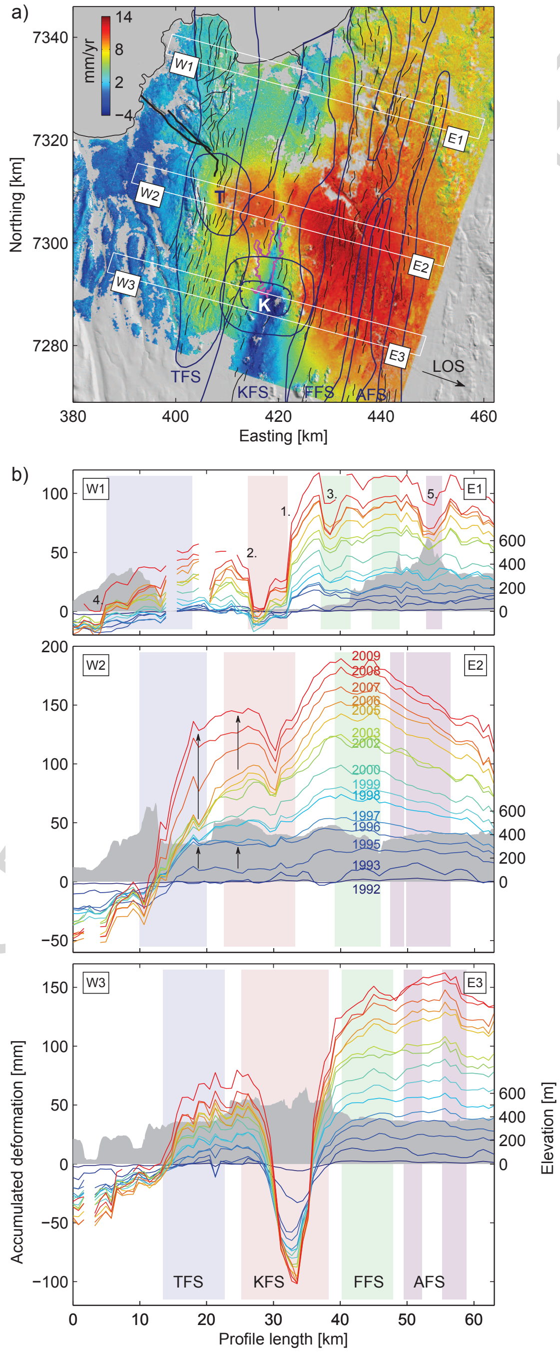

Figure 4: a) Map of the average line-of-sight (LOS) displacement rates for the 1992-2009 time period. The color range is mildly saturated. The Húsavík-Flatey fault (bold black lines) and the fissure swarms (dark blue lines) of Theistareykir (T, TFS), Krafla (K, KFS), Fremrinámur (FFS) and Askja (AFS) are shown. The outline of the 1975-1984 Krafla lava flows are shown in pink (from Sæmundsson et al., 2012). b) The temporal evolution of the deformation along the W-E profiles across the Northern Volcanic Zone. The profile topography is shown in gray and color-shades correspond to the widths of the fissure swarms. Black arrows and numbers are referred to in the text. Profile gaps are caused by an insufficient number of data points in the rate map.

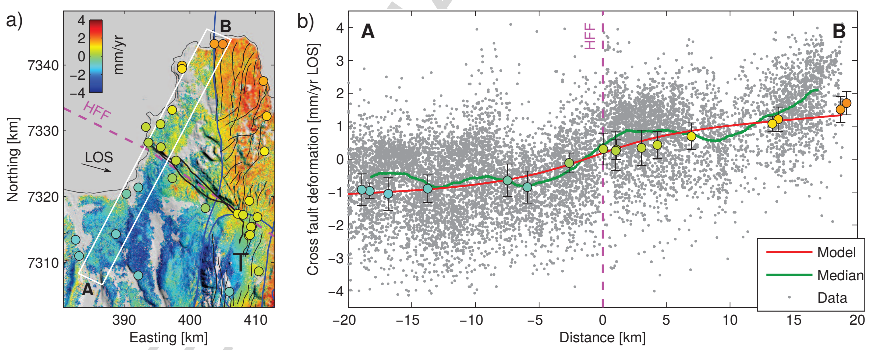

Figure 5: a) LOS InSAR and GPS (filled circles) displacement rates in map view. Bold lines mark HFF fault traces and the model segments are indicated in purple. b) GPS (circles with error bars) and InSAR (gray dots, purple line) in comparison to the model prediction (red line). The data have been corrected for volcanic inflation at Theistareykir (T) using the Mogi model parameters from Metzger et al. (2011).

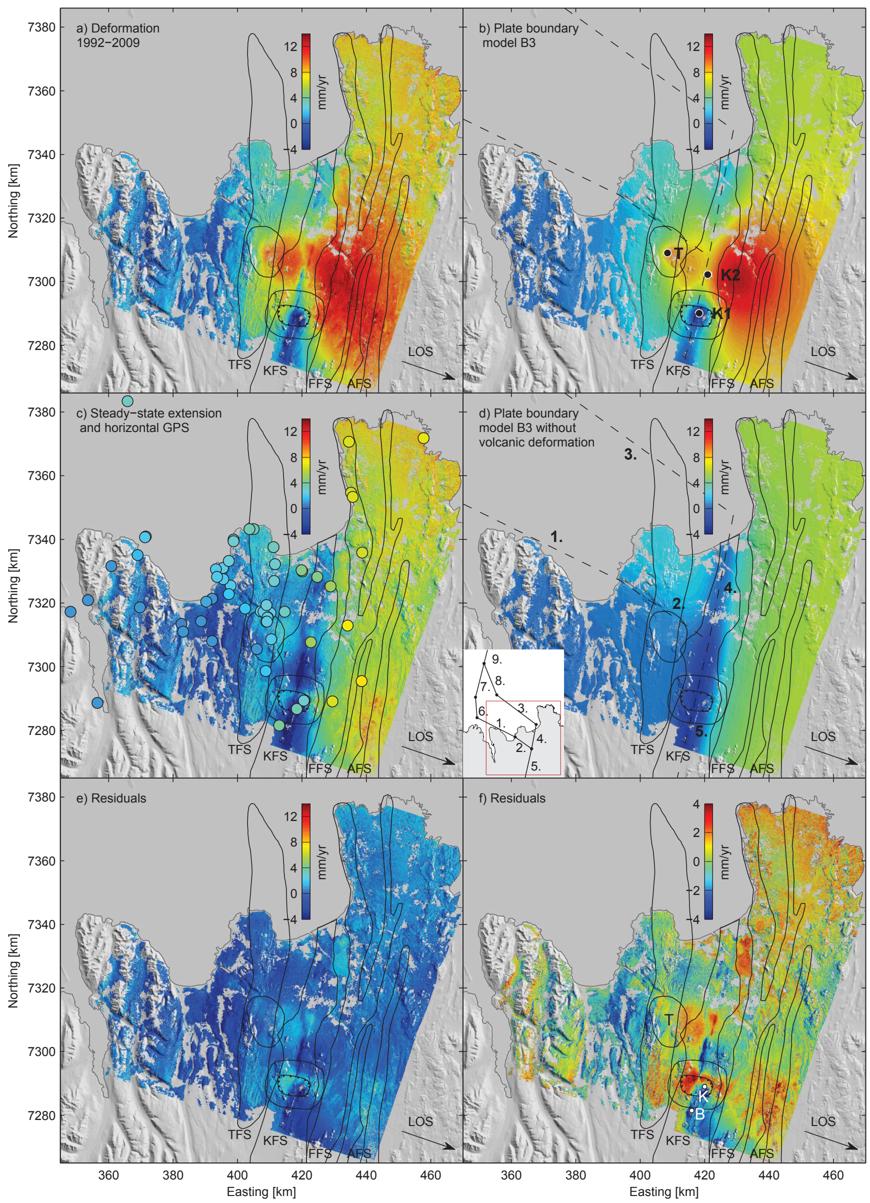

Figure 6: a) Average line-of-sight (LOS) displacement rates w.r.t. stable North American reference frame during 1992-2009. The black lines indicate the fissure swarms of Theistareykir (TFS), Krafla (KFS), Fremrinámur (FFS), and Askja (AFS). b) The predicted displacement rates from model B-3 (Table 2) consisting of three Mogi sources T, K1 and K2 and a set of dislocations representing the plate boundary (dashed lines), see Table 1 for model parameters. c) Same as a), after removing predicted volcanic deformation and in comparison to the horizontal GPS velocities from 1997-2010 (Metzger et al., 2013). d) Predicted displacement rates of the interseismic deformation model B-3. The inset shows the geometry of all nine model segments (the numbers 1 to 9 refer to Table 2). e/f) The residuals of the average displacement, after removing b) from a), given in two different color scales, show unmodeled local deformation, e.g. at the lava flow north of Krafla (K) and at the geothermal fields of Krafla and Bjarnaflag (B).

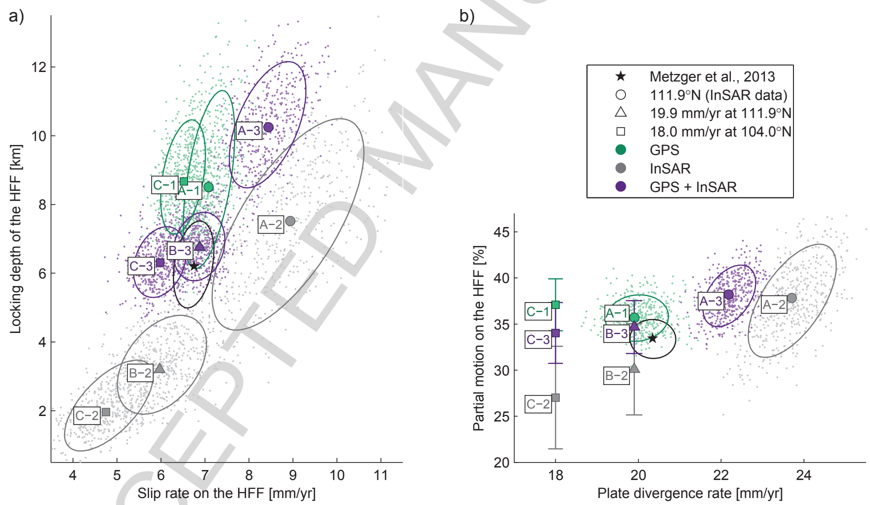

Figure 7: Best-fit solutions and results of uncertainty estimation (including 68%-confidence ellipses) for a) locking depth vs. slip rate of the HFF and b) the amount of slip occurring on the HFF vs. plate divergence using different input data and model constraints. The legend indicates if the plate divergence rate and azimuth were fixed to either the GPS-only solution (A-1) or the MORVEL plate-motion model (DeMets et al., 2010). The reference model (black star, Metzger et al., 2013) is a purely interseismic model without volcanic sources.

Highlights for review

- We present the results of a time-series analysis of 17 years of InSAR and GPS data
- We apply an interseismic plate-boundary model to estimate key kinematic parameters
- The Húsavík-Flatey fault (HFF) accommodates one third of the full transform motion
- The HFF has a slip-rate of 6-9 mm/yr, a locking depth of 6-10 km and a seismic potential of M6.8-7.0
- Most of the present deformation occurs within the Krafla and Theistareykir volcanic systems